Electrochimica Acta 284 (2018) 587–596

Contents lists available at ScienceDirect

Electrochimica Acta

journal homepage: www.elsevier.com/locate/electacta

Zn-Fe-rich granular sludge carbon (GSC) for enhanced electrocatalytic removal of bisphenol A (BPA) and Rhodamine B (RhB) in a continuous-flow three-dimensional electrode reactor (3DER)

Jing Ji [a], Xiu-yan Li [a], Juan Xu [a, b, *], Xue-yuan Yang [a], Hui-shan Meng [a], Zi-run Yan [a]

[a] Shanghai Key Lab for Urban Ecological Processes and Eco-Restoration, School of Ecological and Environmental Sciences, East China Normal University, Shanghai, China
[b] Institute of Eco-Chongming, East China Normal University, Shanghai, China

ARTICLE INFO

Article history:
Received 12 May 2018
Received in revised form
26 July 2018
Accepted 27 July 2018
Available online 30 July 2018

Keywords:
Three-dimensional electrochemical reactor (3DER)
Granular sludge carbon (GSC)
Particle electrode
Sewage sludge

ABSTRACT

Recycling sewage sludge from wastewater treatment plants is one of the most challenging environmental problems. In this work, we develop a one-step facile synthesis method of converting iron-rich sewage sludge into granular sludge carbon (GSC), further applying as particle electrodes in three-dimensional electrochemical reactor (3DER) for wastewater treatment. Iron in sludge and zinc in activator are in-situ loaded on particle electrodes as catalytic ingredients. The prepared GSC under different pyrolysis temperature are characterized to investigate the physical, chemical and electrochemical properties. The treatment performances of GSC as particle electrodes are evaluated by degrading bisphenol A (BPA) and Rhodamine B (RhB) in a continuous-flow 3DER. The stability of the GSC are evaluated and possible reaction mechanism are explored. Results indicate that GSC fabricated are typical macroporous material, exhibiting good electrocatalytic activity. The 500 °C/GSC packed 3DER shows the best performances in contaminants removal, that was attributed to larger specific surface and superior electrochemical properties with cooperation of iron oxide and zinc oxide components. The 500 °C/GSC prepared are proved to be suitable for utilizing as particle electrodes in 3DER. Our work offers a new strategy for sewage sludge reuse and provides a promising future for 3DER applications.

1. Introduction

Sewage sludge is an inevitable byproduct during biological wastewater treatment, which is produced in large amounts around the world [1]. Traditional disposal of sewage sludge by landfill and incineration [2] generates secondary pollution due to the presence of organic compounds, pathogenic microorganisms and potentially toxic matters in the sludge, and consequently threatening public health. Thus, the efficient technology is urgently needed to deal with the sewage sludge properly. In view of rich organic components in sewage sludge, converting waste materials into valuable products offers a superior alternative from the perspective of resource recovery. Novel technologies such as composite, pyrolysis and gasification have been developed for sludge disposal [3,4]. Among these technologies, sludge carbonization to produce activated carbon for environment remediation exhibits high feasibility. It not only reduces sewage sludge efficiently, but also produces functional materials for contaminants removal.

Recently, three-dimensional electrochemical reactor (3DER) has attracted wide interests for its high efficiency, environmental compatibility and easy operation in the decomposition of refractory contaminants such as organic acids, phenolic compounds, dyes and petroleum refinery wastewaters [5]. In the 3DER, granular activated carbon (GAC) was frequently employed as the particle electrodes owing to its fascinating features of low cost, chemical stability and high surface area [6]. The major drawback of GAC is the weak electrocatalytic activity, which would influence the treatment performances of the contaminants during the electrochemical process. Thus, many efforts have been made to modify GAC to improve their catalytic properties. For example, Pd-GAC particles were prepared for catalytical reduction of haloacetic acids by impregnating Pd^{2+} ions onto GAC [7,8]. SnO_2-Sb-doped TiO_2-coated GAC with a high hydroxyl radical yield were synthesized to enhance

* Corresponding author. Shanghai Key Lab for Urban Ecological Processes and Eco-Restoration, School of Ecological and Environmental Sciences, East China Normal University, Shanghai, China.
E-mail address: jxu@des.ecnu.edu.cn (J. Xu).

https://doi.org/10.1016/j.electacta.2018.07.203
0013-4686/

the treatment of Rhodamine B dyeing wastewater [9]. However, these modified GAC of high electrocatalytic activity are either too expensive or too complicated for fabrication, restricting further development and application in wastewater treatment.

The principle of GAC modification as particle electrode in 3DER is loading metallic (including metal oxide) material onto GAC to improve catalytic performance [10]. Recently, the iron oxide have been found effective in heterogeneous Fenton-like oxidation of various organic pollutants. Their superior catalytic behavior could work over a wide pH range [11]. Thus, sewage sludge containing iron might be a suitable precursor of preparing activated carbon particle electrode in 3DER. During the carbonization process, iron can be converted to iron oxide simultaneously, which is loaded in-situ on the sludge derived activated carbon [12,13].

Currently, sludge carbon has been used as heterogeneous catalyst in ozonation and Fenton reaction for the removal of refractory pollutants [14,15]. In general, sludge carbon catalyst was prepared by two steps. Firstly, the sludge was converted to activated carbon by activation and carbonization, following with acid wash to improve carbon content and porosity. Then, the obtained sludge carbon was further treated by surface modification such as loading metals. The procedures are relatively complicated, and moreover, the metals existed in the sludge and $ZnCl_2$ activator are wasted during the acid wash. In fact, when sludge carbon was utilized as particle electrode in 3DER, the demand of carbon content and porosity are not necessary as high as for other application. Too high carbon content would induce internal short circuit and decrease current efficiency. Too high porosity would cause coverage of catalytic sites due to excessive adsorption. Both of the results are not favorable for the contaminants removal. In addition, the sludge carbon in the form of powder cannot be adapted to 3DER. That are difficult to separate from wastewater along with equipment clogging and catalyst loss. Thus, for application in 3DER, it is necessary to transfer powder sludge carbon into granular sludge carbon (GSC).

In this study, GSC was synthesized by iron-rich sewage sludge and served as particle electrode in 3DER for wastewater treatment. $ZnCl_2$ was selected as activator for promoting the aromatization of the carbon skeleton as well as the formation of porous structure [16]. Sewage sludge deserved GSC was fabricated by one-step approach of activation, granulation and carbonization, in-situ utilizing organic matters and iron in sludge and zinc in activator to produce GSC loaded with iron oxide and zinc oxide. To optimize the catalytic performance of the GSC, various temperatures were selected for sludge carbonization. The catalytic activity of the prepared GSC was evaluated by degrading a typical endocrine disruptor bisphenol A (BPA) and a representative dye, Rhodamine B (RhB). The objectives of this study are (1) to fabricate the GSC by iron-rich sludge with a simple one-step approach; (2) to estimate the feasibility of using GSC as particle electrode in 3DER; (3) to compare catalytic performance of GSC fabricated under different conditions; (4) to explore the possible catalytic mechanism of GSC in 3DER. Herein, we report a strategy of fabricating efficient and stable GSC particle electrode of 3DER, offering another possible way of sewage sludge recycling and providing a promising future for 3DER applications.

2. Materials and methods

2.1. Materials and reagents

The sewage sludge collected from Tianshan wastewater treatment plant (Shanghai, China) was pretreated with $FeSO_4$ and $Ca(OH)_2$ before dewatering, enriching high contents of Fe and Ca in the sludge (Table S1). Possible hazardous elements in the sludge including arsenic (As), cadmium (Cd), chromium (Cr), copper (Cu), nickel (Ni) and lead (Pb) were also measured. Results showed that the contents of these elements were lower than 0.1% (except Cu of 0.2%), that was acceptable for preparing environmental materials. The other reagents were purchased from Sinopharm Chemical Reagent Co., China.

2.2. Preparation of GSC

The dewatered sewage sludge was dried at 105 °C for 24 h, then grounded and sieved into a uniform size of 150 mesh screen. $ZnCl_2$ solution (5.0 mol/L, 20 mL) as activation agent and 1 g sodium carboxymethyl cellulose as adhesive were added into 100 g sludge. The mixture was stirred slowly for 12 h at ambient temperature, and then was made into spherical precursors with the diameters of 8 mm by the granulator (LD-88A, Chuangli, China). The obtained particles were dried at 105 °C for 12 h and subsequently pyrolyzed in a tube furnace (GSL-1400X, Kejing, China) at heating rate of 10 °C min^{-1} to the designed temperature (300, 500, 700 and 900 °C) in the presence of N_2 holding for 2 h. After cooling to room temperature, the GSC products were washed with 80 °C distill water until the effluent pH was constant.

2.3. Analytical methods

Element analysis of the raw sewage sludge and GSC were conducted by an elemental analyzer (Vario EL, Elementar, Germany). The hazardous element were determined by inductively coupled plasma atomic emission spectrometer (ICP-AES, ICAP7600, Thermo, USA). The concentrations of metal elements in the effluents were detected by inductively coupled plasma optical emission spectroscopy (ICP-OES, Optima 5300DV, Perkin Elmer, USA). The bulk chemical compositions of the catalysts were determined via an X-ray fluorescence spectrometer (XRF, Axios, PANalytical, Netherlands). Microscopic structure of the GSC samples were observed under a scanning electron microscope (SEM, HITACHI S-4800, HSD, Japan) and high resolution transmission electron microscopy (HRTEM, JEM-2100F, JEOL, Japan). The specific surface area of the samples was measured by Brunauer-Emmett-Teller (BET) method (BELSORP-max. Bel, Japan). The crystal structure of GSC was analyzed by a powder X-ray diffractometer (XRD, Ultima-IV, Rigaku, Japan). Chemical species of Zn, Fe, C and O in GSC were analyzed by X-ray photoelectron spectroscopic (XPS) patterns (Escalab 250Xi, Thermo, USA). BPA concentration was measured by high-performance liquid chromatography (HPLC, 1100 series, Agilent, USA) with an autosampler and an Eclipse Plus C18 column (4.6 × 250 mm, 5 μm, Agilent), and equipped with an UV detector at the wavelength of 225 nm. A quantitative determination of RhB was performed by measuring its absorbance at 554 nm using an UV–visible spectrophotometer (MAPADA, China). Hydroxyl radicals generated during the electrochemical process were detected with electron spin resonance (ESR, EMX-8/2.7, Bruker, Germany). The intermediates of BPA and RhB decomposition were analyzed by gas chromatography-mass spectrometer (GC-MS, 7890A-5975C, Agilent, USA).

The electrochemical property of GSC was analyzed on an electrochemical workstation (CHI 660E, Chenhua, China) using a conventional three-electrode system. A glassy carbon disk (3.0 mm in diameter) coated with various GSC catalysts was used as the working electrode, with Pt wire as the counter electrode and Ag/AgCl electrode as the reference electrode. The cyclic voltammetry (CV) measurements were conducted in BPA (5 μM BPA + 0.1 M PBS), RhB (52.2 μM RhB + 0.05 M Na_2SO_4) and $K_3Fe(CN)_6$ (0.25 mM $K_3Fe(CN)_6$ + 0.05 M Na_2SO_4) solution. N_2 was purged into the solution for 30 min prior to each CV and scanning.

Electrochemical impedance spectroscopy (EIS) were measured in 5 mM $K_3Fe(CN)_6$ containing 0.1 M KCl with frequency ranging from 100 kHz to 10 mHz and amplitude of 10 mV. The conductivity of GSC samples were measured by four-point probe method on a resistivity meter (ST2722-SZ, Suzhou Jingge Electronics, China).

2.4. Continuous-flow 3DER for evaluating the catalytic performance of GSC

The continuous-flow 3DER was a plexiglas rectangular tank with a working volume of 80 mL. The main electrodes including a Ti/RuO_2-IrO_2 anode (100 mm × 30 mm × 1 mm) and a titanium plate cathode with the same dimension (Shuerde, China) were positioned vertically and parallel to each other with an inner gap of 3 cm. The prepared GSC particle electrodes were packed between the anode and cathode. Commercial GAC particle electrodes (Jiacheng Co., Zhejiang, China) and 3DER without particle electrodes (2DER) were also tested for comparison. A peristaltic pump (YZ1515x, Longer, China) was used to pump the simulated wastewater into the bottom of the 3DER. The concentrations of RhB and BPA in influents were 100 mg/L and 20 mg/L, respectively. Na_2SO_4 (0.1 M) was added as electrolyte to enhance the electrochemical process. The flow rate was set as 13.3 mL/min for RhB and 6.67 mL/min for BPA, corresponding to the hydraulic retention time (HRT) of 6 min and 12 min. Air was purged through a microporous aeration stone at the bottom of the influent tank, and the aeration rate was 250 mL/min adjusted by a flowmeter to ensure sufficient dissolved oxygen in influent (8.25 mg/L). The experiments were conducted into two stages: (i) adsorption under the open-circuit condition (0–4 h) and (ii) electrolysis by applying 8 V voltage (4–8 h) using a digital DC power supply (CE0036030S, RainWorm, China). The effluent samples of continuous-flow 3DER were collected at the designed time and filtered through a 0.45 μm nitrocellulose membrane before analysis.

3. Results

3.1. Morphology and texture of GSC

The GSC samples prepared under different temperatures were shown in Fig. 1. The obtained products were designed as 300 °C/GSC, 500 °C/GSC, 700 °C/GSC and 900 °C/GSC, corresponding to the pyrolysis temperature with an average diameter of 6.0, 5.9, 5.0 and 4.8 mm, respectively. There appeared obvious cracks on the surface of 300 °C/GSC. That was due to the incomplete carbonization of cellulose and lignin at low pyrolysis temperature. After elevating pyrolysis temperature to 500 °C, the prepared GSC had certainly complete structure with good mechanical strength. According to the components analysis of GSC listed in Table 1, the volatiles, apparent density and yield decreased with the increasing pyrolysis temperature. That was because organics in the sludge volatilized more thoroughly, and consequently the yield and apparent density decreased. The main components of ash were inorganic salts and oxides which kept stable under the high temperature, leading to the raise of the ash proportion with increasing temperature. It was noticed that, with the raise of pyrolysis temperature, the apparent color of GSC was changing from black into red gradually (Fig. 1). That was related to the speciation of iron oxides, which would be illustrated in section of structure and composition.

SEM results showed that the surface morphology of GSC (Fig. 2a–d) were rougher with irregular cavities compared with the raw sludge (Fig. 2e). The porous surfaces of GSC were created by $ZnCl_2$ and the evaporation/decomposition of organics during the pyrolysis process. The rough surface of the GSC could provide more activated sites for particle electrodes reacting with wastewater. In addition, EDX mapping (Fig. 2f) revealed the homogenous distribution of C, O, Fe and Zn in the GSC, facilitating electrocatalytic process on the particle electrodes for contaminants removal.

The N_2-adsorption/desorption isotherms were measured at

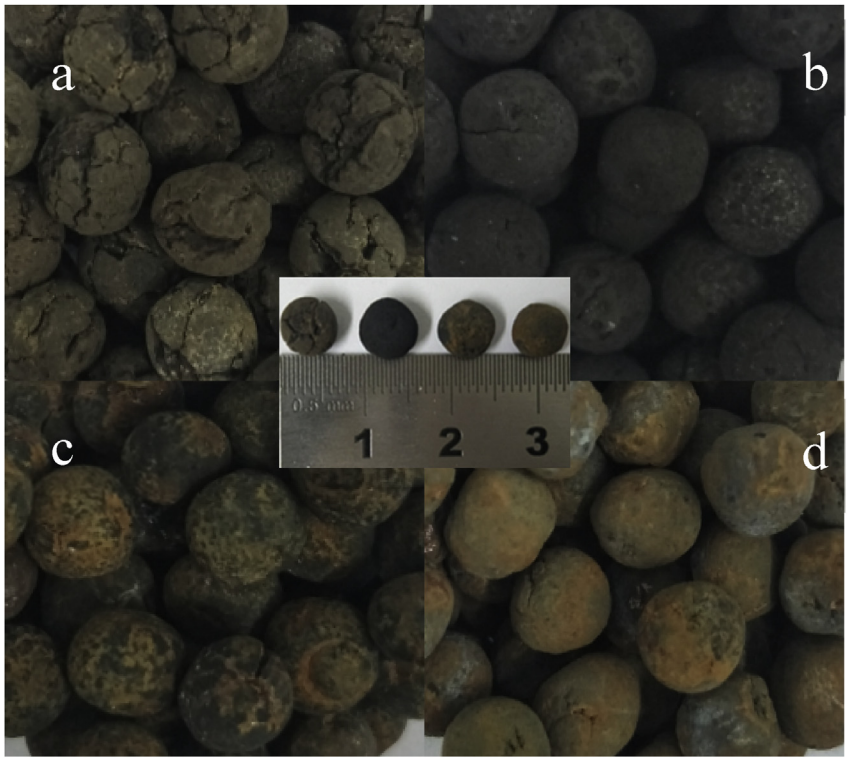

Fig. 1. Images of GSC samples under different carbonization temperature: (a) 300 °C/GSC, (b) 500 °C/GSC, (c) 700 °C/GSC, (d) 900 °C/GSC.

Table 1
Chemical analysis, apparent density and yield of the GSC.

sample	C (%)	H (%)	N (%)	S (%)	Zn (%)	Fe (%)	volatiles (%)	ash (%)	apparent density (g/ml)	Yield(%)
300 °C/GSC	22.99	3.24	2.72	1.13	27.70	14.76	39.5	58.4	0.7182	85.2
500 °C/GSC	16.47	1.40	2.00	1.31	34.67	14.05	32.7	58.6	0.5948	66.2
700 °C/GSC	15.85	0.86	1.31	1.51	31.20	12.75	18.9	79.6	0.5604	56.4
900 °C/GSC	14.44	1.11	0.39	1.93	11.64	15.66	15.5	81.3	0.4920	45.5

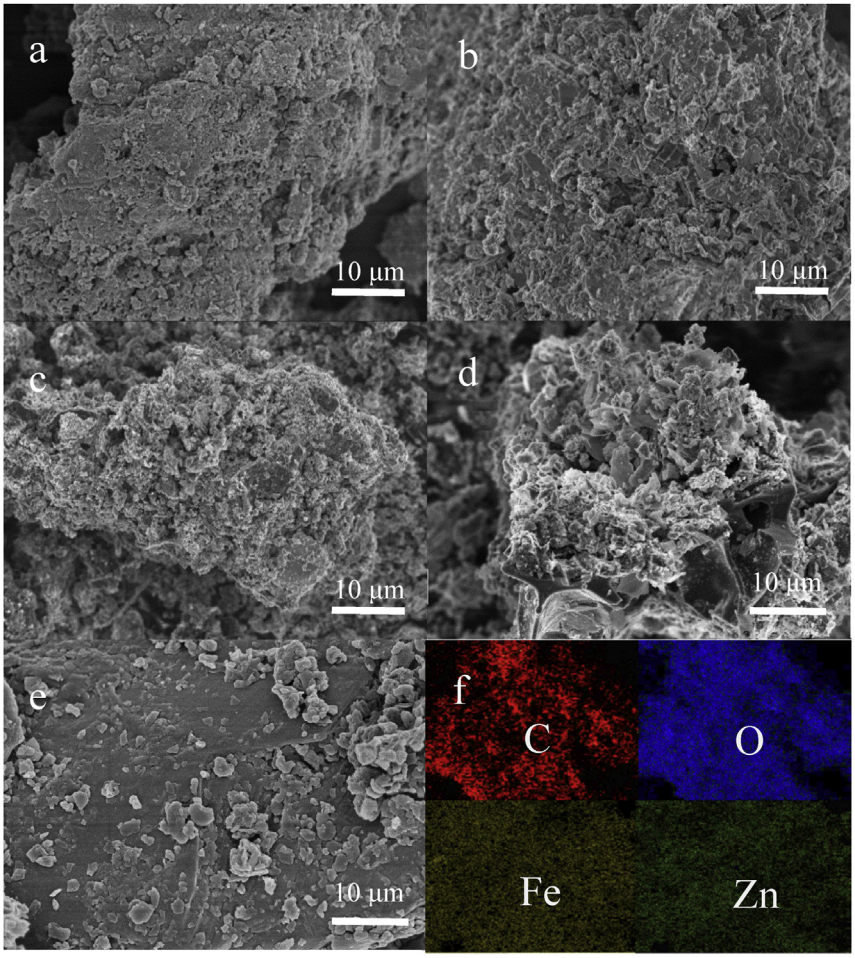

Fig. 2. SEM images of the different GSC samples: (a) 300 °C/GSC, (b) 500 °C/GSC, (c) 700 °C/GSC, (d) 900 °C/GSC, (e) raw sewage sludge and (f) The EDX mapping of the C, O, Fe, and Zn in 500 °C/GSC.

77.3 K to investigate the pore volume and surface area of GSC samples (Fig. S1). According to the IUPAC classification, all of the isotherms belonged to type IV, indicating that the GSC prepared were typical porous material of large-pore. That was attributed to lots of secondary pores formed by the close stack of complex components inside the GSC [17]. As listed in Table 2, the 500 °C/GSC had highest porosity among the GSC samples. The 500 °C/GSC displayed larger specific surface area, which was lowered by the further increase of pyrolysis temperature. That was because 500 °C was sufficient to attain the requisite decomposition of the sewage sludge. Too high sintering temperature would disintegrate the porous structure of GSC, leading to the block of some pores and the drop of the specific surface area [18].

3.2. Structure and composition of GSC

XRD was employed to investigate the structure and crystallinity of the GSC samples. The patterns of the ZnO, graphite, Fe_3O_4 and α-Fe_2O_3 were identified as shown in Fig. 3. The main peaks at $2\theta = 31.7°$, 34.4°, 36.2°, 47.5°, 56.5°, 62.8°, 66.28°, 67.9° and 69.0° were the diffraction of the crystalline planes of the ZnO (JCPDS. Card 80-0075), as follows: (1 0 0), (0 0 2), (1 0 1), (1 0 2), (1 1 0), (1 0 3), (2 0 0), (1 1 2) and (2 0 1). The conventional broad peak at $2\theta = 26.6°$ was the characteristic diffraction peak of graphite, corresponding to the (0 0 3) plane. The characteristic diffraction peaks at $2\theta = 30.1°$, 35.4°, 56.9°, and 62.6° corresponded to (2 2 0), (3 1 1), (5 1 1) and (4 4 0) planes of the Fe_3O_4 (JCPDS. Card 72-2303). Furthermore, the diffraction peaks at $2\theta = 33.2°$, 35.6°, 40.9° and 54.1° were associated with (1 0 4), (1 1 0), (1 1 3) and (1 1 6) planes of α-Fe_2O_3 (JCPDS. Card 33-0664).

These XRD results suggested the discrepancy of the GSC samples pyrolyzed under different temperatures. There was no obvious diffraction signal in 300 °C/GSC, as this temperature was not high enough to completely crystallize carbon and metal oxides. The

Table 2
Textural properties of the GSC.

sample	average pore size (nm)	specific surface area (m^2/g)	pore volume (cm^3/g)
300°C/GSC	120.473	29.267	0.0882
500°C/GSC	79.540	132.150	0.263
700°C/GSC	86.316	92.782	0.200
900°C/GSC	105.990	10.195	0.0270

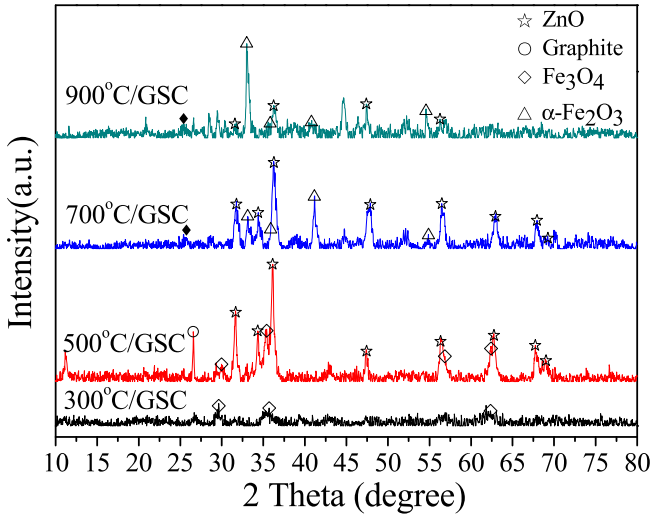

Fig. 3. XRD patterns of the GSC samples.

diffraction peaks of ZnO crystals were observed in 500 °C/GSC, 700 °C/GSC and 900 °C/GSC. However, the diffraction intensity of ZnO decreased with the increase of pyrolysis temperature due to volatilization of ZnO. That would also influence the morphology of the GSCs due to the enlarged pore size. The crystalline structure of GSC samples were also characterized by HRTEM as shown in Figs. S2a–d. The clear lattice fringes with a spacing of 0.287 nm corresponding to the (1 0 0) planes of the ZnO was found in 500 °C/GSC, 700 °C/GSC and 900 °C/GSC samples (Fig. S2e). For the carbon component, a weak peak appeared at $2\theta = 26°$ in 700 °C/GSC and 900 °C/GSC, corresponding to the characteristic diffraction of amorphous carbon. That meant the low graphite crystallization under relatively higher calcination temperature [19]. In comparison, 500 °C/GSC comprised more graphite crystallites of good chemical resistance and electrical conductivity, which was ideal material for electrodes fabrication [20]. This result was further proved by the conductivity measurement listed in Table S2. The 500 °C/GSC had the highest conductivity of 52.63 S/m, which was higher than the other GSCs. For Fe component, 300 °C/GSC was mainly consisted of typical non-crystalline Fe_3O_4, while 500 °C/GSC was mainly consisted of Fe_3O_4 crystallites. With the increase of calcination temperature, Fe_3O_4 was converted to α-Fe_2O_3, which dominated 700 °C/GSC and 900 °C/GSC. The XRD results agreed with the HRTEM analysis. The 0.475 nm lattice fringes ascribed to (1 1 1) planes of Fe_3O_4 nanosheets was observed in 500 °C/GSC (Fig. S2f). Meanwhile, 0.203 nm lattice fringes ascribed to the (2 0 2) planes of Fe_2O_3 were observed in both 700 °C/GSC and 900 °C/GSC (Fig. S2g).

The chemical composition of GSC samples were further investigated by XPS analysis. The survey spectra of GSC were displayed in Fig. 4a. Obviously, the Zn 2p, Fe 2p, O 1s and external C 1s peaks appeared in the spectra of GSC. As shown in Fig. 4b, the peaks of Zn 2p3/2 and Zn 2p1/2 were located at 1022.18 and 1045.30 eV. The peaks were positively shifted compared to the previous studies, which identified the peaks of Zn 2p3/2 and Zn 2p1/2 in ZnO at 1021.35 eV and 1044.39 eV [21].

XPS results also revealed the differences in the oxidation state of the iron as shown in Fig. 4c. The Fe 2p levels were split into 2p3/2 and 2p1/2 doublets due to the spin-orbit coupling. For 700 °C/GSC and 900 °C/GSC, the peaks of Fe 2p3/2 and Fe 2p1/2 were observed at 712.14 and 725.97 eV. There also existed a charge transfer satellite peak of Fe 2p3/2 located at 720.49 eV. The satellite peak was the fingerprints of the electronic structures of Fe(III), implying that Fe_2O_3 was prevalent in 700 °C/GSC and 900 °C/GSC [22]. Such a satellite structure disappeared in the spectrum of 500 °C/GSC, leaving Fe 2p3/2 and Fe 2p1/2 main peaks at 711.20 and 725.14 eV. The disappeared satellite peaks indicated the presence of Fe(II) in the form of Fe_3O_4 [23]. This results agreed with the XRD analysis, which also confirmed the existence of Fe_3O_4 in 500 °C/GSC. Moreover, the binding energy of Fe 2p electrons in 500 °C/GSC shifted to the direction of higher energy compared to that of standard Fe_3O_4 with the Fe 2p3/2 and Fe 2p1/2 peaks at 710.6 and 724.1 eV [22]. The increased binding energy of Fe 2p was possibly owed to the electronic environment changes of Fe_3O_4 in the GSC such as the conjunction of Fe_3O_4-ZnO [21]. Similar results were also observed in the spectrum of 300 °C/GSC, in which the Fe 2p3/2 and the Fe 2p1/2 peaks located at 711.17 eV and 724.74 eV.

From Fig. 4d, the XPS spectra of O 1s can be divided into seven peaks for the GSC samples with the binding energies of 530.31 ± 0.08, 531.58 ± 0.17, 532.91 ± 0.10, 532.50 ± 0.04, 531.00 ± 0.24, 532.74 ± 0.09 and 531.42 ± 0.11 eV. The O 1s peaks located at 530.31 and 531.58 eV were assigned to the Fe-O and Zn-O bonds. The peak at 532.91 eV belonged to H-O-H from the adsorbed water molecules from surroundings [24]. The binding energies of C-O, Ca-O, Si-O/Mg-O and Al-O were assigned at 532.50, 531.00, 532.74 and 531.42 eV, respectively. The peak area and relative percentages were calculated in Table S3. Less adsorbed oxygen was detected in 300 °C/GSC than the other GSCs. That was not favorable for the contaminants removal. It was because chemisorbed oxygen could promote the production of H_2O_2 in the reaction system and improve the yield of hydroxyl radicals [25]. The fraction of Zn-O dropped with the increment of pyrolysis temperature, while Fe-O exhibited a rising trend. High temperature induced evaporation of ZnO but facilitated formation of iron oxides [26]. The peak relative percentages of C-O, Ca-O, Si-O/Mg-O and Al-O were similar for the GSCs samples.

3.3. Electrocatalytic properties of GSC

The electrochemical behavior of the four GSC particle electrodes in BPA and RhB were investigated by CV measurement with 20 consecutive cycles of scan. Fig. 5a–d presented CVs of glassy carbon electrode coated with GSC recorded in BPA solution. No peaks was observed in the CV of 300 °C/GSC. 500 °C/GSC showed a peak at 0.277 V with the peak current of 8.83 μA, related to the oxidation of BPA. The anode peak current declined for 700 °C/GSC (2.31 μA at 0.238 V) and 900 °C/GSC (1.477 μA at 0.654 V). The 500 °C/GSC showed higher anodic current response, suggesting stronger electrochemical oxidation to BPA. However, the redox peaks of BPA were not obvious for all the GSC particle electrodes, implying that

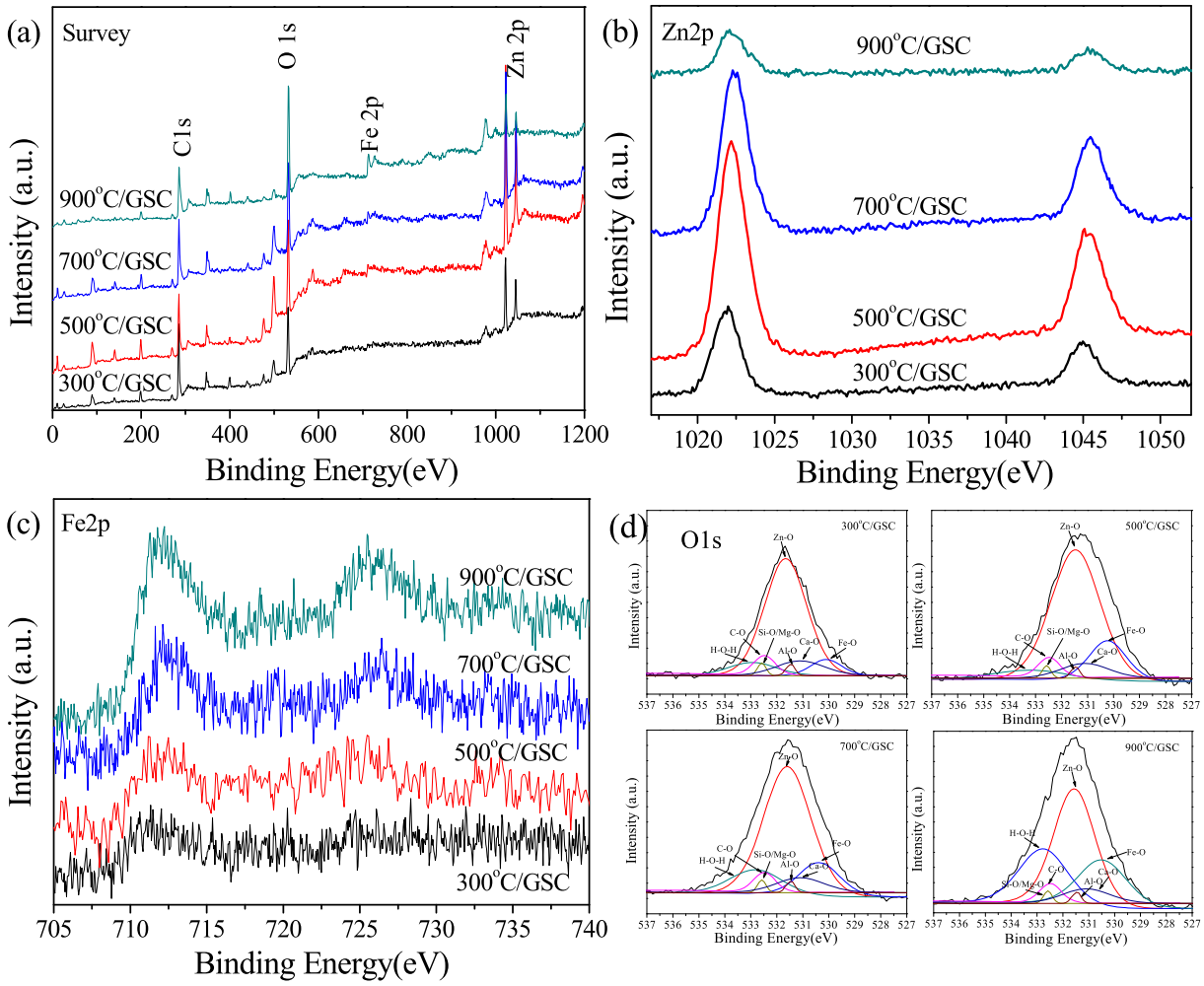

Fig. 4. (a) XPS survey of the GSC samples; XPS patterns of (b) Zn 2p, (c) Fe 2p and (d) O 1s.

the direct electrochemical oxidation of BPA on the GSC particle electrodes was not significant.

As shown in Fig. 5e–h, redox peaks of RhB were much clear than those of BPA. High peak intensities were observed for 500 °C/GSC with two anodic peaks and one cathodic peak. For 300 °C/GSC, 700 °C/GSC and 900 °C/GSC, the intensities of redox peaks declined. The 500 °C/GSC exhibited the highest anodic peak current (988 μA) compared to 300 °C/GSC (541 μA), 700 °C/GSC (641 μA) and 900 °C/GSC (634 μA). The results indicated that electrochemical oxidation of RhB on 500 °C/GSC electrode was more intensive than on the other GSC electrodes.

CV measurement was also performed in $K_3Fe(CN)_6$ solution. As displayed in Fig. 6a, redox peaks were very weak for 300 °C/GSC. Significantly enhanced peak intensities were observed for 500 °C/GSC with anodic and cathodic peaks located at 0.361 and 0.083 V. For 700 °C/GSC and 900 °C/GSC, the intensities of redox peaks decreased. The 500 °C/GSC exhibited the highest anodic peak current (22.4 μA) compared with 300 °C/GSC (11.3 μA), 700 °C/GSC (18.6 μA) and 900 °C/GSC (16.7 μA). The results indicated that heterogeneous electron transfer rate of 500 °C/GSC was more rapid than the other GSC samples, thus accelerating the electrochemical process effectively.

Fig. S3a showed CVs of $K_3Fe(CN)_6$ solution under gradual scan rates (from 15 to 100 mV/s). Both cathodic and anodic peak currents increased linearly with the scan rate (Fig. S3b), suggesting that the electron transfer at 500 °C/GSC electrode was a typical surface-confined electrochemical behavior. The electrochemically active surface area (ECSA) of the electrodes for GSC could be estimated by CV measurement according to Randles-Sevcik equation [10]:

$$Ip = 2.69 \times 10^5 n^{3/2} A D^{1/2} \upsilon^{1/2} C \quad (1)$$

where Ip is the anodic peak current (A), n is the number of transferred electrons, A is the ECSA of the electrode (cm^2), D is the diffusion coefficient of the molecule ($6.70 \times 10^{-6}\ cm^2\ s^{-1}$) [10], υ is the scan rate (V/s), and C is the bulk reduced-species concentration (mol/mL). From the slope of the Ip - $\upsilon^{1/2}$ relation as shown in Fig. S3b, the ECSAs of the 300 °C/GSC, 500 °C/GSC, 700 °C/GSC and 900 °C/GSC were calculated to be 0.41, 0.81, 0.67 and 0.61 cm^2, which were comparable to the electrode materials prepared in other studies such as graphene-nanosheet clusters (0.102 cm^2) and exfoliated graphite nanoplatelets (0.18 cm^2) [10,27]. Results demonstrated that 500 °C/GSC had the largest area of electrochemical active surface for contaminants oxidation.

EIS could be applied for investigating the electron transfer properties of the GSC particle electrodes, which was shown in Fig. 6b. The Nyquist plots of GSC samples consisted of two parts: semicircle pattern at high frequency range and a straight line at low frequency range, which corresponded to the charge transfer reaction and diffusion of the electrode-electrolyte interface

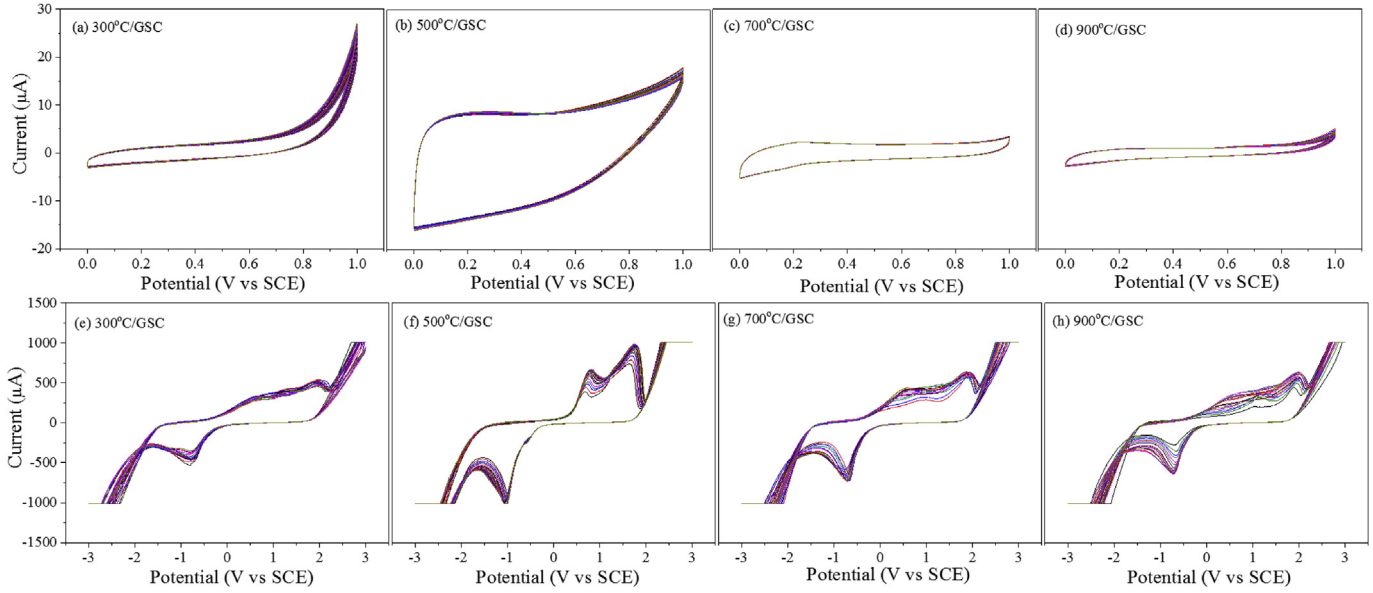

Fig. 5. CVs of GSC samples recorded in 5 μM BPA +0.1 M PBS, scan rate: 0.1 V/s (a) 300 °C/GSC, (b) 500 °C/GSC, (c) 700 °C/GSC, (d) 900 °C/GSC with 20 consecutive cycles of scan; CVs of GSC samples recorded in 52.2 μM RhB + 0.05 M Na_2SO_4, scan rate: 0.1 V/s (e) 300 °C/GSC, (f) 500 °C/GSC, (g) 700 °C/GSC, (h) 900 °C/GSC with 20 consecutive cycles of scan.

respectively. The smaller arc radius for 500 °C/GSC particle electrode clearly indicated the reduced electron transfer resistance. That was beneficial to reaction occurrence on 500 °C/GSC particle electrodes. These results agreed well with the CV analysis.

3.4. GSC as particle electrodes for contaminants removal in 3DER

As shown in Fig. 7, the 3DER packed with GSC achieved better treatment performance than 3DER packed with pure GAC and 2DER without particle electrodes. The GSC fabricated effectively enhanced the electrochemical oxidation of the contaminants.

For the treatment of BPA (Fig. 7a), the removal efficiency kept stable during the adsorption of 4 h. The average removal efficiency were 22.13%, 30.87%, 28.58% and 26.48% for 300 °C/GSC, 500 °C/GSC, 700 °C/GSC and 900 °C/GSC. 500 °C/GSC showed the highest capacity in BPA adsorption, due to the relatively higher specific surface area. When the voltage was applied, the removal efficiency of the 3DERs increased rapidly. During the electrolysis stage, the 500 °C/GSC packed 3DER obtained the highest BPA removal efficiency ranged from 84.07 to 89.56%. The removal efficiency were 13.05–25.76%, 72.78–81.42% and 64.30–73.25% for 3DER packed with 300 °C/GSC, 700 °C/GSC and 900 °C/GSC. 300 °C/GSC showed no significant electrocatalytic performance in BPA removal, due to scarcity of crystalline structure. For GAC, the removal efficiency of BPA decreased rapidly from 63.47% to 25.49%. The results demonstrated that 500 °C/GSC had a superior electrocatalytic activity for BPA removal.

Fig. 7b showed the RhB removal in 3DER packed with different GSCs. During the adsorption stage, the average removal efficiency were 7.44%, 14.06%, 10.57% and 10.34% for 300 °C/GSC, 500 °C/GSC, 700 °C/GSC and 900 °C/GSC. Applying external voltage significantly strengthened the removal of RhB in 3DER due to electrochemical oxidation. However, the removal efficiency of RhB during electrolysis was not as stable as that of BPA, decreasing to various degrees with the treatment time. For 500 °C/GSC and 700 °C/GSC, the removal efficiencies were similar (about 80%) in the initial time of electrolysis (4.5–5 h), higher than the other particle electrodes. Afterwards, the removal efficiencies declined rapidly for all the particle electrodes. After treating for 8 h, the removal efficiencies decreased to 23.53%, 40.75%, 36.56% and 40.10% for 300 °C/GSC, 500 °C/GSC, 700 °C/GSC and 900 °C/GSC. 500 °C/GSC always showed better RhB treatment performance compared to the other particle electrodes.

The discrepancy in the removal efficiency of BPA and RhB might be due to different removal mechanisms of the two contaminants in 3DER. According to CV analysis, direct electrochemical oxidation on the GSC particle electrodes was not significant for BPA removal, but was important for RhB removal. The deteriorated treatment performance of RhB was induced by the coverage of activated sites on particle electrodes, considering the high RhB concentration in influents (100 mg/L) and the short HRT of 3DER (6 min). The excessively adsorbed RhB could not be degraded by electrochemical oxidation promptly, leading to RhB accumulation and blockage of the particle electrodes. That would directly reduce the removal efficiency of RhB during continuous operation. This problem could be resolved by optimizing the operating parameters of the 3DER such as adjusting HRT and voltage in the further study.

For applications in wastewater treatment, the stability of the GSC was also estimated. The concentrations of main metal elements in the effluents of 3DER were summarized in Table S4. Results indicated that the concentrations of Zn, Fe, Ca and Cu in the 3DER effluents were lower than integrated wastewater discharge standard (GB 8978-1996). The concentrations of Al and Mg were below the detection limitation of 0.05 mg/L. The main metal composition of GSC before and after electrochemical reaction were shown in Fig. 8. The metal composition in GSC had no significant changes after reaction. That meant the catalytic components in GSCs were stable without obvious loss during continuous operation. The content of Zn in 500 °C/GSC was the highest with the value of 34.5%, followed by Fe of 13.7%. The corresponding oxides of the two metals played important roles in catalytical oxidation process. The compounds of Ca, Si, Al, Mg provided strong skeleton support to maintain the granular state of the GSC.

To further prove the degradation of BPA and RhB, the effluents of 3DER were analyzed by GC-MS. Possible intermediates generated during the treatment process were identified and listed in Tables S5 and S6. Results indicated that the molecular structure of BPA and

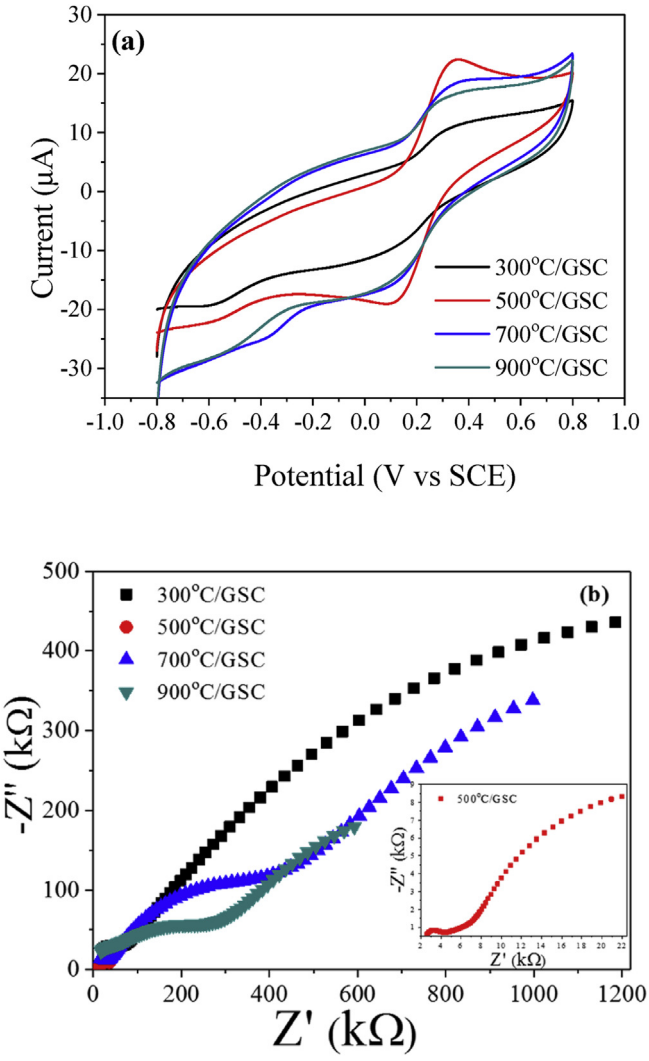

Fig. 6. (a) CVs of GSC samples recorded in 0.25 mM $K_3Fe(CN)_6$ + 0.05 M Na_2SO_4; (b) EISs of GSC samples recorded in 5 mM $K_3Fe(CN)_6$ + 0.1 M KCl.

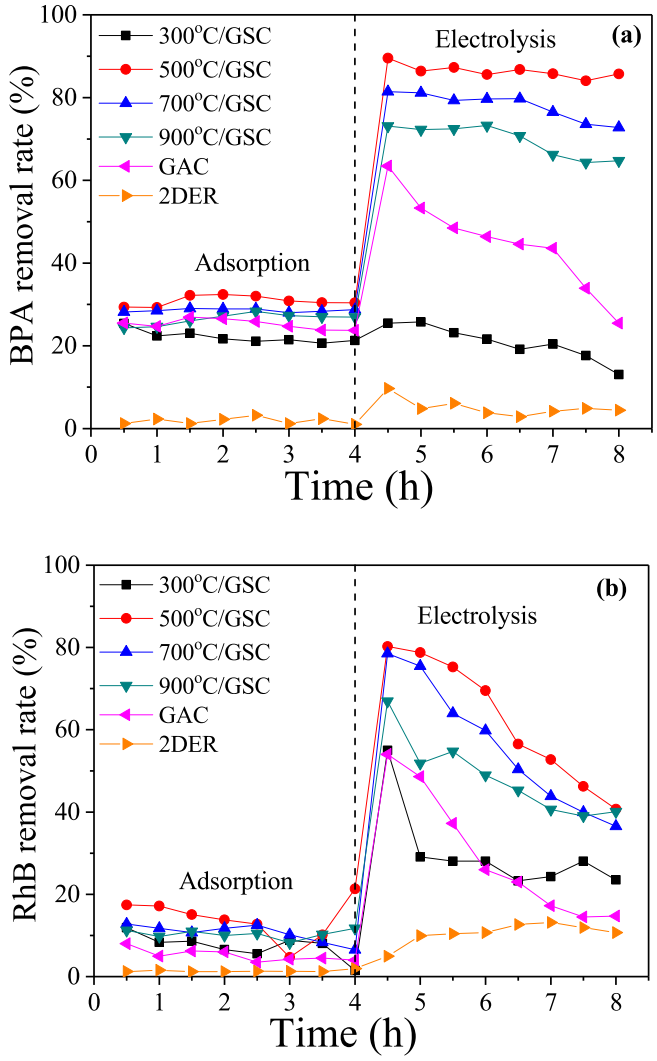

Fig. 7. (a) BPA (BPA 20 mg/L, HRT 12 min, voltage 8 V, pH, 7) and (b) RhB (RhB 100 mg/L, HRT 6 min, voltage 8 V, pH 7) removal rate in the continuous-flow 3DER packed with different particle electrodes.

RhB altered, producing various intermediates during electrolysis. Generally, the prepared 500 °C/GSC exhibited efficient and stable performance in wastewater treatment. They were suitable for application in 3DER as particle electrodes with potential of engineering application.

4. Discussion

Previous studies indicated that the hydroxyl radical (•OH) played an important role in the electrochemical oxidation of contaminants in 3DER. In this work, the •OH in the aquatic phase was detected by using the •OH scavenger DMPO and ESR technique [9]. As shown in Fig. 9, typical ESR spectra of the DMPO-•OH adduct with a 1:2:2:1 quartet were observed in the 3DER packed with 500 °C/GSC, 700 °C/GSC and 900 °C/GSC [28]. It demonstrated that the electrogeneration of •OH occurred on the GSC electrodes when external voltage was applied. Lacking of metal oxide crystals, 300 °C/GSC was not capable of generating detectable •OH. Moreover, it was worth noting that 900 °C/GSC other than 500 °C/GSC achieved the highest ESR intensity for the DMPO-•OH spectrum. The •OH quantification by terephthalic acid fluorescent probe method (Fig. S4) were in consistency with ESR results. However, for the treatment performance, 500 °C/GSC showed better electrocatalytic activity for oxidizing BPA and RhB than the other GSCs. Possible reasons were deduced as follows.

Oxidation of organic pollutants on particle electrodes involved O-transfer reactions, via the production of adsorbed •OH generated from water discharge reactions (eqs (2) and (3)), where S[ ] represents the surface sites where the •OH species can be adsorbed [20]:

$$S[\ ] + H_2O \rightarrow S[\bullet OH] + H^+ + e^- \quad (2)$$

$$S[\bullet OH] + R \rightarrow S[\ ] + RO + H^+ + e^- \quad (3)$$

It was demonstrated that ZnO could promote the water discharge reaction by providing more water adsorption sites [29]. Water molecules could be accumulated at the surface of the particle electrodes rapidly due to the high content of ZnO in 500 °C/GSC. Consequently, with the catalysis of iron oxides, •OH generated was bound on the surface of the particle electrodes rather than releasing into the aquatic phase. As shown in Fig. 9, the intensity of free •OH increased with the decreasing ZnO amounts in particle electrodes. The results implied the significant roles of surface •OH

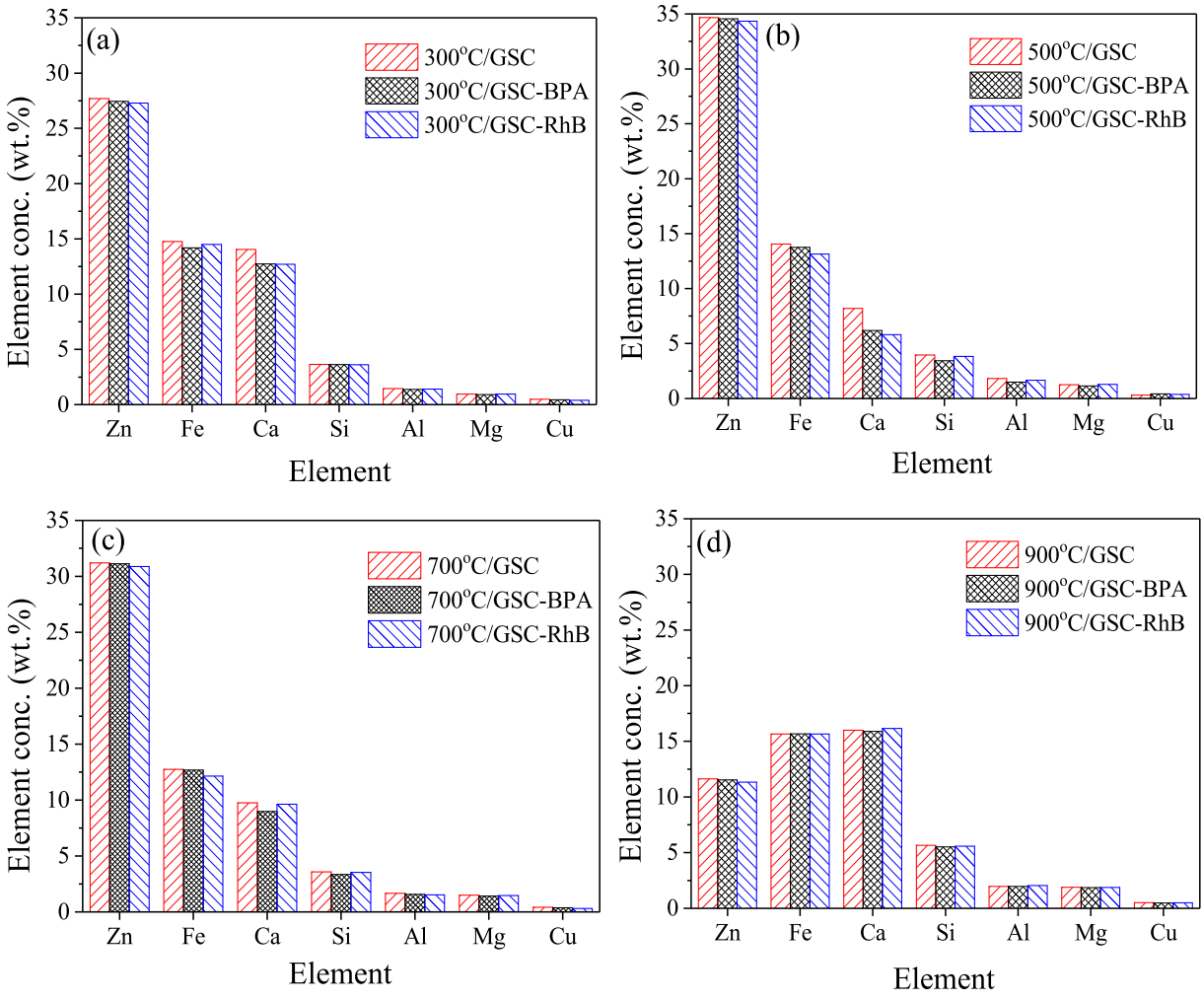

Fig. 8. Metal compositions (wt. %) of GSCs before and after reaction with BPA and RhB by XRF analysis.

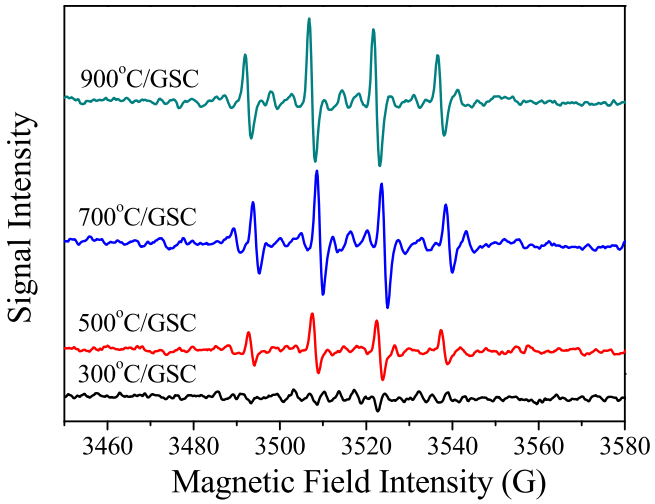

Fig. 9. DMPO spin-trapping ESR spectra of •OH radicals in the 3DER packed with different GSC particle electrodes.

on particle electrodes in contaminants removal, which was also found in other studies [30,31]. High content of ZnO was the main reason for increasing surface-bound •OH in 500 °C/GSC particle electrodes.

The GSC was fabricated from Fe-rich sewage sludge by activation and pyrolysis. The Fe existed in the sewage sludge and Zn from $ZnCl_2$ activation were retained in GSC as the active catalytic ingredients. As particle electrodes of 3DER, GSC with in-situ loaded Fe-Zn oxides showed better electrocatalytic activity than pure GAC. Especially, 500 °C/GSC exhibited excellent physical, chemical and electrochemical properties, degrading the contaminants by adsorption, direct oxidation and indirect oxidation. The larger specific surface area of 500 °C/GSC could enhance the adsorption process. The adsorption was responsible for improving the concentration of contaminants substrate at the interface of particle electrodes, accelerating the degradation rate. For the direct oxidation, both large ECSA and the presence of graphite crystallites in 500 °C/GSC facilitated electron transfer between the contaminants and the electrode, leading to enhanced organics oxidation. For the indirect oxidation, the cooperation of ZnO and Fe_3O_4 in 500 °C/GSC had better catalytic activity due to enhanced water adsorption and the catalysis of Fe_3O_4 involved in producing surface-bound •OH for contaminants removal.

Moreover, GSC of granular state facilitated the separation of catalyst and wastewater in 3DER, avoiding catalyst loss and equipment clog. The facile synthesis method included only one-step of activation, granulation and carbonization, savings the production cost to a great extent. Our work offered a new strategy for sewage sludge reuse and provided a promising future for 3DER applications.

5. Conclusions

In this study, sewage sludge-derived GSC was synthesized via a one-step facile method and packed in a 3DER as particle electrodes for wastewater treatment. Results indicated that 500 °C/GSC exhibited excellent physical, chemical and electrochemical properties. The mechanism could be elucidated as: (1) The large specific surface area enhanced the adsorption process, accelerating the contaminants degradation; (2) The high ECSA and the presence of graphite crystallites facilitated electron transfer between the contaminants and the electrodes; (3) The cooperation of ZnO and Fe_3O_4 improved the production of strong oxidizing species eg. surface-bound •OH. 3DER packed with 500 °C/GSC showed prominent electrochemical oxidation performance towards both RhB and BPA. The GSC was ideal material of particle electrodes in 3DER. Our work offered a new strategy for sewage sludge reuse and provided a promising future for 3DER applications.

Acknowledgements

The authors wish to thank National Natural Science Foundation of China (51708224) for the support of this study.

Appendix A. Supplementary data

Supplementary data related to this article can be found at https://doi.org/10.1016/j.electacta.2018.07.203.

References

[1] F. Wang, K. Shih, X. Lu, C. Liu, Mineralization behavior of fluorine in perfluorooctanesulfonate (PFOS) during thermal treatment of lime-conditioned sludge, Environ. Sci. Technol. 47 (2013) 2621–2627.
[2] L. Gu, N. Zhu, H. Guo, S. Huang, Z. Lou, H. Yuan, Adsorption and Fenton-like degradation of naphthalene dye intermediate on sewage sludge derived porous carbon, J. Hazard. Mater. 246–247 (2013) 145–153.
[3] W.Y. Xu, D. Wu, Comprehensive utilization of the pyrolysis products from sewage sludge, Environ. Technol. 36 (2015) 1731–1744.
[4] J. Villaseñor, L. Rodríguez, F.J. Fernández, Composting domestic sewage sludge with natural zeolites in a rotary drum reactor, Bioresour. Technol. 102 (2011) 1447–1454.
[5] C. Zhang, Y. Jiang, Y. Li, Z. Hu, L. Zhou, M. Zhou, Three-dimensional electrochemical process for wastewater treatment: a general review, Chem. Eng. J. 228 (2013) 455–467.
[6] L.Y. Wei, S.H. Guo, G.X. Yan, C.M. Chen, X.Y. Jiang, Electrochemical pretreatment of heavy oil refinery wastewater using a three-dimensional electrode reactor, Electrochim. Acta 55 (2010) 8615–8620.
[7] X. Zhao, A.Z. Li, R. Mao, H.J. Liu, J.H. Qu, Electrochemical removal of haloacetic acids in a three-dimensional electrochemical reactor with Pd-GAC particles as fixed filler and Pd-modified carbon paper as cathode, Water Res. 51 (2014) 134–143.
[8] R. Mao, X. Zhao, H.C. Lan, H.J. Liu, J.H. Qu, Graphene-modified Pd/C cathode and Pd/GAC particles for enhanced electrocatalytic removal of bromate in a continuous three-dimensional electrochemical reactor, Water Res. 77 (2015) 1–12.
[9] X. Li, Y. Wu, W. Zhu, F. Xue, Y. Qian, C. Wang, Enhanced electrochemical oxidation of synthetic dyeing wastewater using SnO_2-Sb-doped TiO_2-coated granular activated carbon electrodes with high hydroxyl radical yields, Electrochim. Acta 220 (2016) 276–284.
[10] C.e. Zou, B. Yang, D. Bin, J. Wang, S. Li, P. Yang, C. Wang, Y. Shiraishi, Y. Du, Electrochemical synthesis of gold nanoparticles decorated flower-like graphene for high sensitivity detection of nitrite, J. Colloid Interface Sci. 488 (2017) 135–141.
[11] G.K. Zhang, Y.Y. Gao, Y.L. Zhang, Y.D. Guo, Fe_2O_3-pillared rectorite as an efficient and stable fenton-like heterogeneous catalyst for photodegradation of organic contaminants, Environ. Sci. Technol. 44 (2010) 6384–6389.
[12] S.J. Yuan, X.H. Dai, Facile synthesis of sewage sludge-derived mesoporous material as an efficient and stable heterogeneous catalyst for photo-Fenton reaction, Appl. Catal. B Environ. 154 (2014) 252–258.
[13] S.J. Yuan, X.H. Dai, Facile synthesis of sewage sludge-derived in-situ multi-doped nanoporous carbon material for electrocatalytic oxygen reduction, Sci. Rep. 6 (2016).
[14] G. Wen, Z.H. Pan, J. Ma, Z.Q. Liu, L. Zhao, J.J. Li, Reuse of sewage sludge as a catalyst in ozonation - efficiency for the removal of oxalic acid and the control of bromate formation, J. Hazard. Mater. 239 (2012) 381–388.
[15] Y.T. Tu, S.H. Tian, L.J. Kong, Y. Xiong, Co-catalytic effect of sewage sludge-derived char as the support of Fenton-like catalyst, Chem. Eng. J. 185 (2012) 44–51.
[16] K.M. Smith, G.D. Fowler, S. Pullket, N.J.D. Graham, Sewage sludge-based adsorbents: a review of their production, properties and use in water treatment applications, Water Res. 43 (2009) 2569–2594.
[17] Y. Areerob, J.Y. Cho, W.K. Jang, W.C. Oh, Enhanced sonocatalytic degradation of organic dyes from aqueous solutions by novel synthesis of mesoporous Fe_3O_4-graphene/ZnO@SiO_2 nanocomposites, Ultrason. Sonochem. 41 (2018) 267–278.
[18] T. Yang, A.C. Lua, Textural and chemical properties of zinc chloride activated carbons prepared from pistachio-nut shells, Mater. Chem. Phys. 100 (2006) 438–444.
[19] L. Ai, H. Huang, Z. Chen, X. Wei, J. Jiang, Activated carbon/$CoFe_2O_4$ composites: facile synthesis, magnetic performance and their potential application for the removal of malachite green from water, Chem. Eng. J. 156 (2010) 243–249.
[20] C.A. Martínez-Huitle, M.A. Rodrigo, I. Sirés, O. Scialdone, Single and coupled electrochemical processes and reactors for the abatement of organic water pollutants: a critical review, Chem. Rev. 115 (2015) 13362–13407.
[21] Z. Lu, X. Zhao, Z. Zhu, M. Song, N. Gao, Y. Wang, Z. Ma, W. Shi, Y. Yan, H. Dong, A novel hollow capsule-like recyclable functional ZnO/C/Fe_3O_4 endowed with three-dimensional oriented recognition ability for selectively photodegrading danofloxacin mesylate, Catal. Sci. Technol. 6 (2016) 6513–6524.
[22] T. Yamashita, P. Hayes, Analysis of XPS spectra of Fe^{2+} and Fe^{3+} ions in oxide materials, Appl. Surf. Sci. 254 (2008) 2441–2449.
[23] M. Sun, X.R. Ru, L.F. Zhai, In-situ fabrication of supported iron oxides from synthetic acid mine drainage: high catalytic activities and good stabilities towards electro-Fenton reaction, Appl. Catal. B Environ. 165 (2015) 103–110.
[24] J.A. Ramos Guivar, E.A. Sanches, F. Bruns, E. Sadrollahi, M.A. Morales, E.O. López, F.J. Litterst, Vacancy ordered γ-Fe_2O_3 nanoparticles functionalized with nanohydroxyapatite: XRD, FTIR, TEM, XPS and Mössbauer studies, Appl. Surf. Sci. 389 (2016) 721–734.
[25] X. Li, S. Sun, X. Zhang, G. Liu, C.R. Zheng, J. Zheng, D. Zhang, H. Yao, Combined electro-catazone/electro-peroxone process for rapid and effective Rhodamine B degradation, Separ. Purif. Technol. 178 (2017) 189–192.
[26] S. Xue, H. Zhuang, C. Xue, L. Hu, B. Li, S. Zhang, Effect of temperature on structural and morphologic properties of ZnO films annealed in ammonia ambient, J. Electron. Mater. 36 (2007) 502–506.
[27] J. Lu, I. Do, L.T. Drzal, R.M. Worden, I. Lee, Nanometal-decorated exfoliated graphite nanoplatelet based glucose biosensors with high sensitivity and fast response, ACS Nano 2 (2008) 1825–1832.
[28] K. Anzai, T. Aikawa, Y. Furukawa, Y. Matsushima, S. Urano, T. Ozawa, ESR measurement of rapid penetration of DMPO and DEPMPO spin traps through lipid bilayer membranes, Arch. Biochem. Biophys. 415 (2003) 251–256.
[29] F. Rong, J. Zhao, P.P. Su, Y. Yao, M.R. Li, Q.H. Yang, C. Li, Zinc-cobalt oxides as efficient water oxidation catalysts: the promotion effect of ZnO, J. Mater. Chem. A 3 (2015) 4010–4017.
[30] T.M. El-Morsi, W.R. Budakowski, A.S. Abd-El-Aziz, K.J. Friesen, Photocatalytic degradation of 1,10-dichlorodecane in aqueous suspensions of TiO(2): a reaction of adsorbed chlorinated alkane with surface hydroxyl radicals, Environ. Sci. Technol. 34 (2000) 1018–1022.
[31] E.R. Carraway, A.J. Hoffman, M.R. Hoffmann, Photocatalytic oxidation of organic acids on quantum-sized semiconductor colloids, Environ. Sci. Technol. 28 (1994) 786.